Contents lists available at ScienceDirect

Sensors and Actuators: B. Chemical

From fundamental materials chemistry to sensing applications: Unravelling the water adsorption mechanism of a luminescent optical fibre sensor membrane

Guillermo Cruz-Quesada [a], Beatriz Rosales-Reina [a], Diego López-Torres [b], Santiago Reinoso [a], María Victoria López-Ramón [c], Gurutze Arzamendi [a], César Elosua [b,*], Maialen Espinal-Viguri [a,*], Julián J. Garrido [a,*]

[a] *Institute for Advanced Materials and Mathematics (INAMAT2) & Departamento de Ciencias, Public University of Navarre (UPNA), Campus de Arrosadía, 31006 Pamplona, Spain*
[b] *Institute of Smart Cities (ISC) & Departamento de Ingeniería Eléctrica, Electrónica y de Comunicación, Public University of Navarre (UPNA), Campus de Arrosadía, 31006 Pamplona, Spain*
[c] *Departamento de Química Inorgánica y Orgánica, Facultad de Ciencias Experimentales, University of Jaén, 23071 Jaén, Spain*

A R T I C L E   I N F O

A B S T R A C T

This work provides insight into the correlation between the luminescent response of a water-vapour optical fibre sensor and the textural properties of its lanthanide-doped silica coating. To this end, a library of 16 silica xerogels derived from combinations between 2 lanthanide dopants (Eu^{III}, Tb^{III}) and 8 antenna ligands was synthesised and characterised by photoluminescence spectroscopy and N_2 and CO_2 adsorption-desorption isotherms, among others. Based on the best luminescent response and most-suited porous texture, the material doped with Tb^{III} and 2,2'-(4-(2-Ethoxyethoxy)pyridine-2,6-diyl)bis(4,5-dihydrooxazole) was selected to construct the probe. A film of this material was affixed to a commercial silica fibre by dip-coating and the resulting sensor was tested in a climatic chamber with relative humidity ranging from 20 to 90% to obtain normalised time-response and calibration curves at three temperatures. The response was linear up to certain water-vapour concentrations, beyond which abruptly changed to polynomial, acting against the sensor resolution. The adsorption mechanism was elucidated by comparing the isosteric enthalpies of adsorption calculated from the sensor calibration curves to those determined from the monolith water-vapour isotherms, revealing that capillary condensation in the membrane mesopores was the key phenomenon leading to the response deviating from linearity.

1. Introduction

Porous silica xerogels (XGs) are known for their easy sol-gel synthesis and customised chemical and textural properties. This versatility makes them promising materials for a wide range of applications, from the most conventional (catalysts, adsorbents) to the most sophisticated (e.g., electronics). Due to their structural and thermochemical stability, they are also used as matrices to host a variety of functional substances conferring additional properties to the material. Beyond these characteristics, they show additional features suitable to develop coatings for optical fibre sensors (OFS), such as a refractive index analogous to that of optical fibres; transparency in a wide wavelength range, and the possibility of fine-tuning the porous texture and the surface chemistry by including functional guests in their matrix.

Luminophores are ideal functional guests to endow XG host matrices with optical properties. This strategy opens a wide field of research on the sensing response of the resulting materials because the XG porosity and surface chemistry directly affects the luminophore response by influencing the sensitivity towards target analytes. Lanthanide ions (Ln) are widely known for their characteristic luminescent emission originating from forbidden electronic transitions within shielded 4f and 5d orbitals, leading to small absorption coefficients and low emission rates.

To overcome these drawbacks, they are usually sensitised through chelating antenna ligands bearing chromophores based on conjugated pi-systems, which collect photons upon excitation to transfer charge to the emissive centre [1,2].

Luminescence is one of the transduction mechanisms on which OFS can be based [3]. The emission intensity and lifetime relate to changes in external parameters, allowing the development of pH, temperature, vapours, or humidity sensors [4–8]. The latter has drawn attention due to their application in many industrial processes, such as pharmaceutical, manufacturing, food processing, and paper production [9–11]. Humidity can affect the quality standards of goods as exemplified by some food types, which need constant humidity to avoid spoilage before consumption [12]. Furthermore, the air's relative humidity can significantly impact many physicochemical processes of industrial interest [13,14], making its monitorisation a relevant task for production.

The dependence of the sensor response on the analyte concentration has been widely studied in luminescence-based OFS, but little is currently known about the influence on the signal of the mechanism governing the analyte adsorption on the coating surface. On this ground, this work was conceived to explore the correlation between the response of a water-vapour OFS and the textural properties of the luminescent XG used as the sensitive coating. Silica films have been previously used to successfully detect the presence of water [15–18], but studies on the prediction of the sensor response and the water adsorption mechanism are yet to be developed for luminescence-based OFS. Thus, we decided to prepare a catalogue of XGs with the desired porosity and surface chemistry and endow them with luminescence through doping with Ln^{III} ions and antenna ligands (AL). More specifically, two series of Eu^{III}- or Tb^{III}-doped XGs, each comprising eight materials varying in the AL type, were prepared, and the most suited in terms of porosity and luminescent emission was fully characterised and used as a coating to construct a luminescence-based humidity OFS. To evaluate its sensitivity, reproducibility, and reversibility towards humidity, calibration curves were obtained for the OFS at three different temperatures and water-vapour adsorption-desorption isotherms were registered for a monolith of the doped XG. The information gathered from these two techniques indicates that the coating luminescence decay relates to the concentration of adsorbed water and has allowed us to propose a plausible mechanism for the adsorption process with capillary condensation as the key factor.

2. Experimental

2.1. Preparation of Ln-AL xerogels

Fig. 1 schematises the preparation of the 16 Ln-doped XGs in this work and the collection of 8 AL used to sensitise the Ln emissive centres (see sections S1.1 and S1.2 for further experimental details). The selected ligands with a central pyridinic ring as a common feature (pyridyl groups are well-established chromophores for Ln-sensitisation [1]) are soluble in hydroalcoholic mixtures and provide a variety of chelating coordination modes, from N,N,N- or O,N,O-tridentate to N,O- or O,O-bidentate.

Ln-AL materials were obtained as monoliths following a sol-gel approach adapted from our previous works [19]. Briefly, a 0.01 M aqueous AL solution (1.000 mL) was added dropwise to a 0.01 M aqueous solution (1.000 mL) of $Ln(NO_3)_3 \cdot 6\ H_2O$ (Ln = Tb, Eu) and the resulting mixture was added to a vessel containing tetraethoxysilane (TEOS, 7.495 mL) and ethanol (9.210 mL) under stirring. Then, water (1.295 mL) was added to a total volume of 20.000 mL (TEOS:ethanol: water molar ratio of 1:4.75:5.5). The sols, the pH of which depended on the AL nature, were placed in a thermostatised oven at 333 K until gelation. The gels were cured for one week with ethanol and finally allowed to dry at atmospheric conditions, obtaining the monolith. Pristine TEOS xerogels without any Ln or AL dopants were analogously synthesised at two different pH values to obtain a set of reference materials.

2.2. Optical fibre sensor construction

After characterising the monoliths to select the most-suited materials to build the sensors in terms of porous texture and luminescent emission (Section 3.2), Ln-AL thin films were deposited onto the tips of commercial 1000 μm core plastic-clad silica fibres (1000UMT with numerical aperture of 0.39, purchased from ThorLabs Inc.) with a cladding thickness of 35 ± 15 μm and a High -OH doping to ensure UV transmission. To couple the highest possible luminescence emission, the fibre ends were tapered into a conical geometry (scanning electron micrograph in Fig. 1) that has been demonstrated optimal for luminescence-based sensors [20]. For the tapering process, the tip of a fibre pigtail was first cut and polished to obtain a smooth, perpendicular surface; then, the fibre was placed in a dip-coater and its planar end was subjected to 40 consecutive immersion-withdrawal cycles in HF (constant speed rates of 100 and 1 mm·min^{-1}, respectively), and finally, the resulting tapered fibre end was cleaned with ethanol and water [21].

To deposit Ln-AL films by dip-coating, the tapered fibres were immersed for 10 s into sol-gel mixtures at 75% of the gelation time to ensure optimal rheological properties [22,23]. The fibres were then pulled out at a constant speed of 150 mm·min^{-1} and the emission spectra were registered to confirm film deposition (photonic experimental setup in Fig. S1). This sequence was repeated until maximising the intensity of the luminescent signal, which was in all cases achieved after the third sequence repetition (no significant increase of the most intense luminescent maxima was observed upon the third immersion). The resulting sensor was stored for 2 days under controlled atmosphere (298 K, 40% humidity) for the gelation process to complete. The thickness of the resulting layer is 109.2 ± 13.4 nm, as determined by ellipsometry on a film deposited onto a silicon wafer following the same procedure used to construct the sensor.

3. Results and discussion

3.1. Characterisation of Ln-AL xerogels

The Ln-AL luminescent response was preliminarily inspected with the bare eye through irradiation with a UV lamp for thin-layer chromatography to discriminate the most-suited materials before performing a full characterisation (Fig. S2). The materials Eu-FPA, Eu-3MPA, Tb-3MPA, Eu-3APA and Tb-3APA were straightforwardly discarded because of their barely perceptible or negligible emission. In the case of Tb-FPA, its luminescence was reasonable upon drying the monolith under vacuum as shown in Fig. S2.a, but abruptly decayed when it was exposed to the atmospheric humidity (Fig. S2.b). This behaviour led us to discard this material due to not fulfilling the requirement needed for our type of sensor of being gradually deactivated with increasing water vapour concentration. Although showing intense luminescence, Ln-DPA were also discarded because the low AL solubility in the XG matrix rendered heterogeneous monoliths. Ln-PB, Ln-CA, Ln-3OHPA and Ln-6OHPA met the required criteria for phase homogeneity, transparency, and intense emission, but the latter exhibited blue luminescence associated with the emission of the free ligand rather than the characteristic red or green emission of Eu^{III} and Tb^{III}. In contrast to the sharp and intense Ln emission peaks, those originating from hydroxypicolinates alone are known to be weaker and much broader [24], which makes these bands unsuitable for finely monitoring intensity variations as a response to external stimuli. This fact, together with the compositional heterogeneity arising from the presence of different luminophores in a single material, prevented us from selecting Eu-6OHPA for the OFS construction. After this preliminary test, Ln-PB, Ln-CA, and Ln-3OHPA were the materials chosen for further characterisation.

Fig. 2 displays the room-temperature photoluminescence spectra of the selected materials. The excitation spectra were first obtained to determine the excitation wavelength required to optimise the Ln-
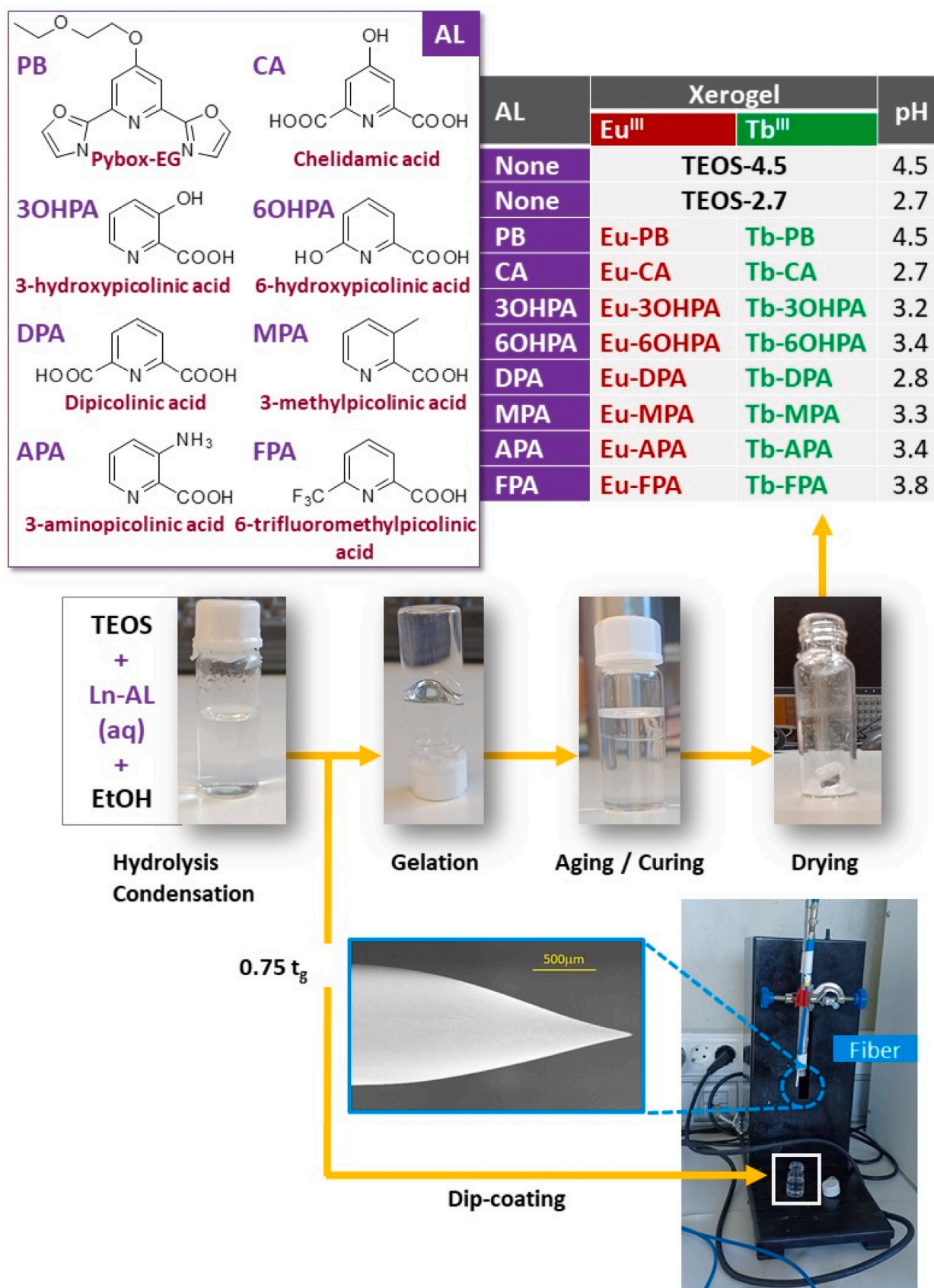
Fig. 1. Scheme of the chelating AL molecules, synthesis of Ln-AL materials, and fibre coating set-up in this work.
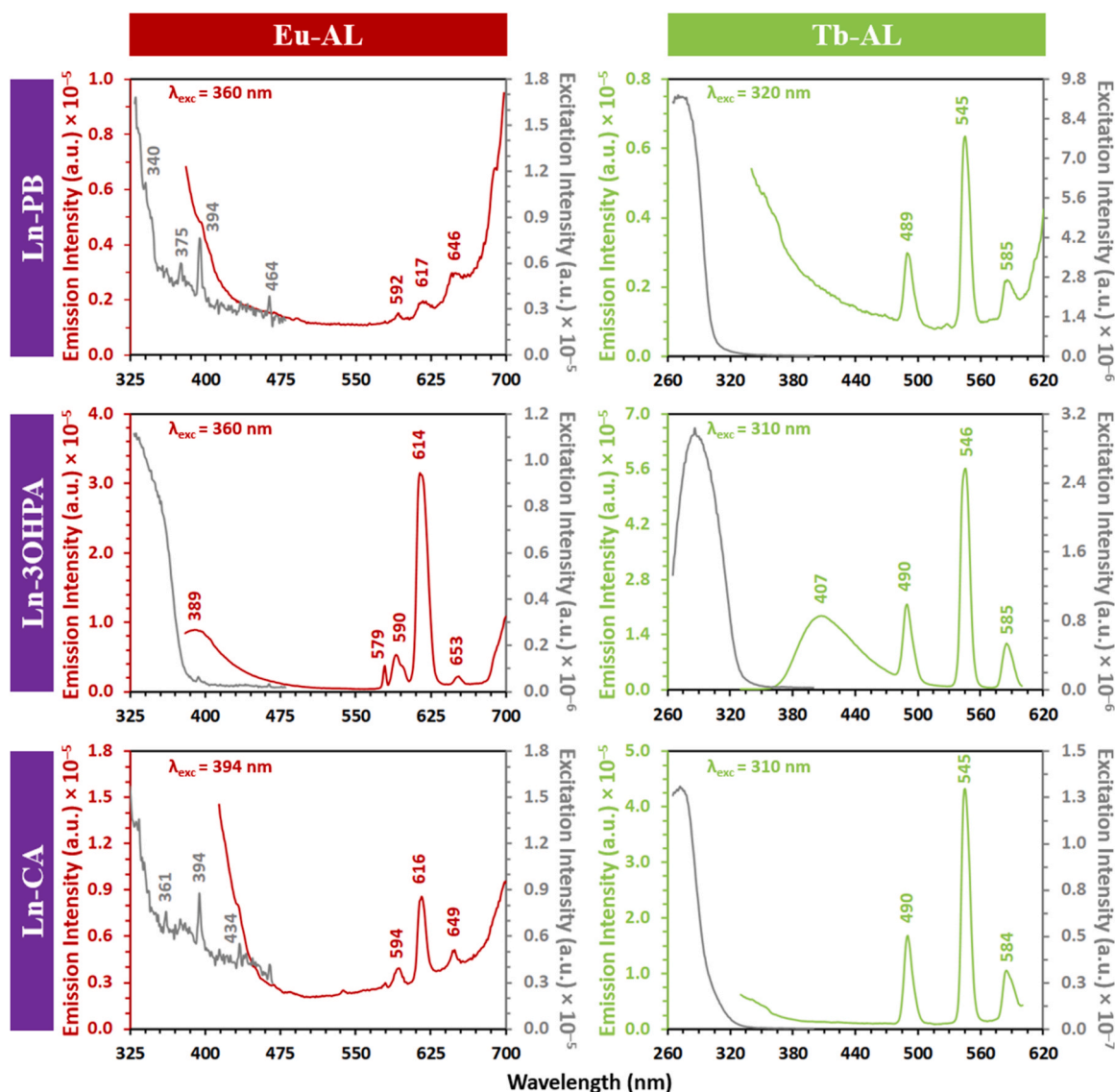
Fig. 2. Room-temperature excitation and emission spectra of Ln-PB, Ln-3OHPA, and Ln-CA.

emission while avoiding spectra overlapping. The emission spectra show the characteristic bands expected for each Ln ion: i) 590, 615 and 650 nm for Eu^{III}, corresponding to $^5D_0 \rightarrow ^7F_j$ transitions ($J = 1$, 2, and 3, respectively), and ii) 490, 545 and 585 nm for Tb^{III}, corresponding to $^5D_4 \rightarrow ^7F_j$ transitions ($J = 6$, 5, 4, respectively) [25]. In all cases, the most intense emission peaks were those at 615 nm for Eu^{III} and 545 nm for Tb^{III} regardless of AL. Comparing the spectra shows that the Tb-CA and Tb-PB emissions are more intense than those of their Eu-counterparts, although the highest intensity corresponds to Eu-3OHPA. However, Ln-3OHPA materials display a blue emission band (Eu^{III}: 389 nm, Tb^{III}: 407 nm) associated with the free ligand, which indicates some degree of compositional heterogeneity as commented above for Ln-6OHPA. Moreover, the bidentate nature of 3OHPA might not fully prevent molecular oscillators (water, ethanol) from quenching the luminescence by incorporation into the Ln coordination sphere, in contrast to the coordinative saturation that the tridentate CA or PB can afford. These two aspects combined led us to discard Ln-3OHPA xerogels for the OFS construction at this stage.

Fig. 3 shows the N_2 isotherms (77 K) of the selected Ln-AL materials compared to those of their TEOS references (semilogarithmic scale depiction in Fig. S3), while Table S1 compiles the textural parameters determined from the adsorption branches. TEOS-4.5 exhibits a mixed

isotherm type that can be best described as IV(a)-I(b) according to the IUPAC classification. It is characteristic of micro-mesoporous materials, as evidenced by the positive slope of the adsorption branch at low relative pressures ($p/p_0 < 0.30$), the hysteresis loop between ~ 0.42 and 0.65 p/p_0, and the absence of any adsorption in the macroporous range (0.8 to 0.95 p/p_0) [26]. Increasing the sol acidity is known to be detrimental to the condensation of colloids, preventing the formation of mesopores and leading to narrower micropores as the pH decreases. This agrees with what is observed for TEOS-2.7, which shows a type I(a) isotherm (reaching a *plateau* at low relative pressures upon a sharp knee) associated with microporous materials showing negligible mesoporosity. Consistently, fewer amounts of adsorbed N_2 and lower pore volumes are observed.

The incorporation of Ln and AL guests induces significant changes in the porous texture of the XG host matrices as indicated by the marked differences between the TEOS and Ln-AL isotherms. Regardless of the pH, all luminescent materials adsorb less amount of N_2 than their references, having substantially lower specific surface areas and pore volumes. For Ln-PB, this fact is mainly due to the cancellation of mesoporosity accompanied by a slight decrease in the microporous domain when Tb^{III} is used as the dopant. Accordingly, Tb-PB shows a type I(a) isotherm whereas that of Eu-PB (reaching saturation through a
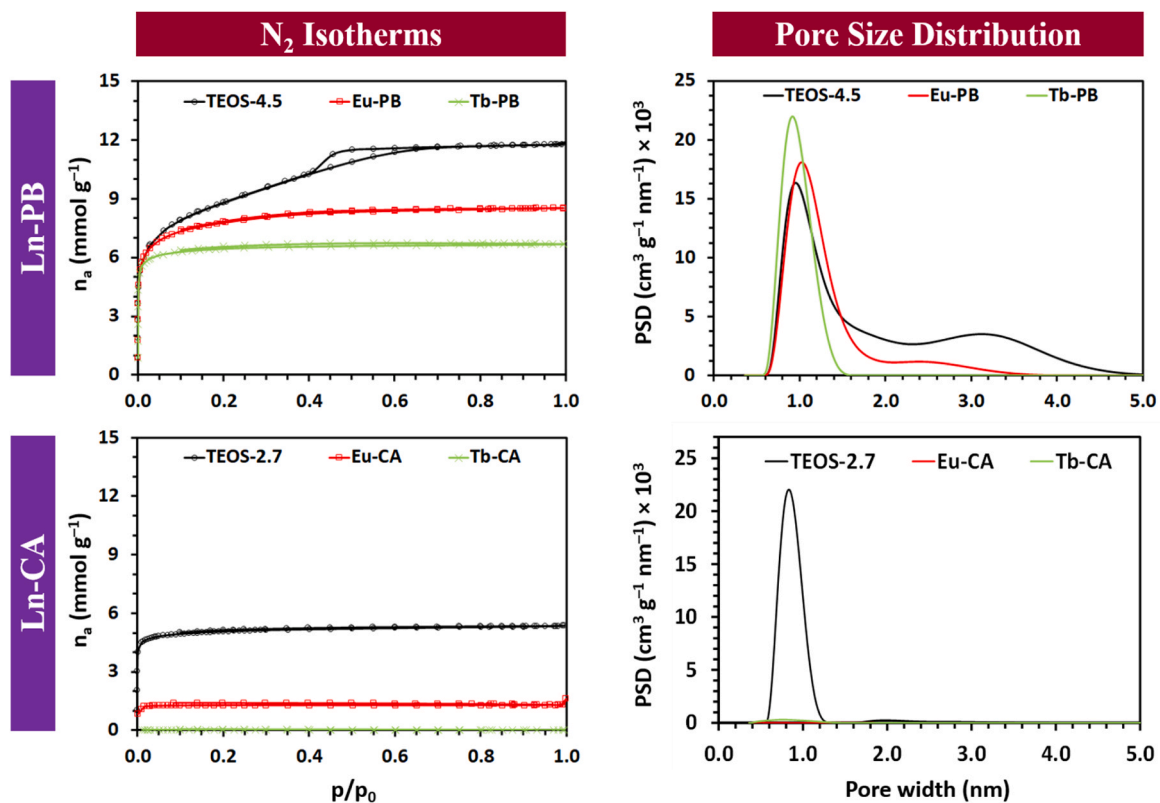
Fig. 3. N_2 isotherms and pore size distribution of Ln-PB and Ln-CA compared to those of their references.
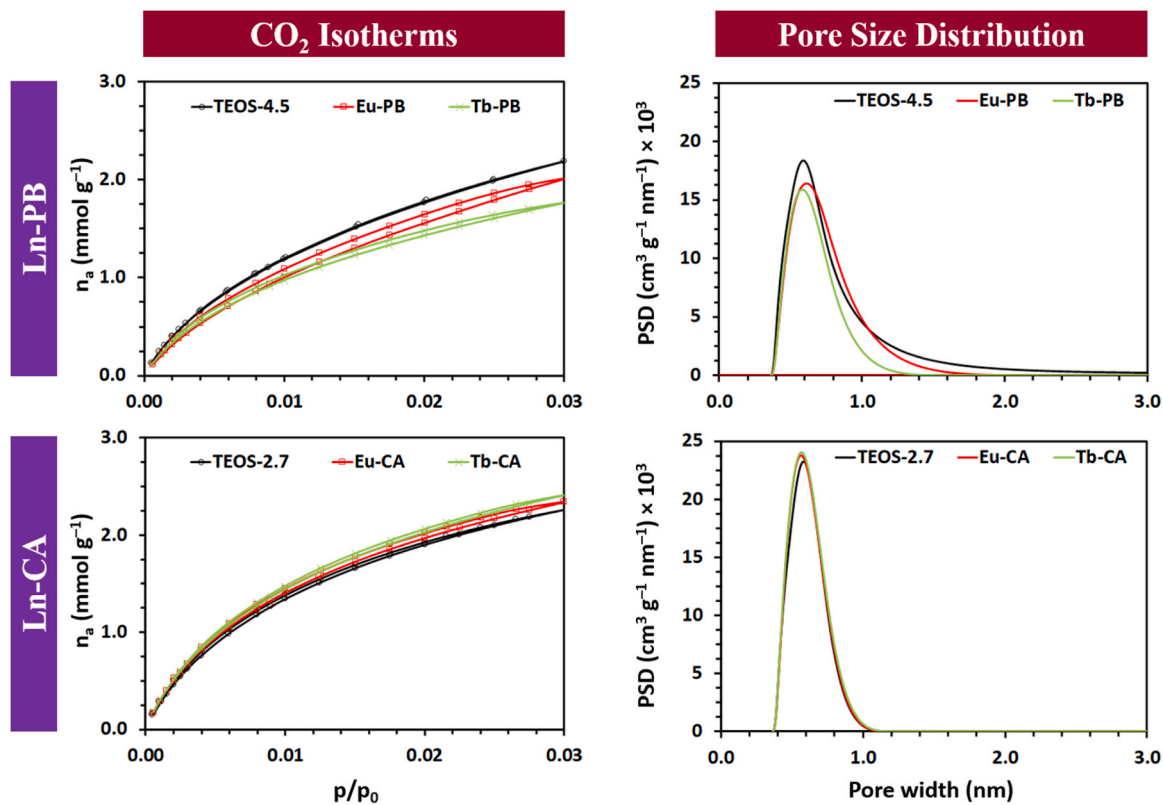

Fig. 4. CO_2 isotherms and pore size distribution of Ln-PB and Ln-CA compared to those of their TEOS references.

smooth slope beyond a flat knee) corresponds to the type I(b), characteristic of microporous materials with a slight volume of mesopores ($\phi >$ 1 nm). Compared to TEOS-4.5, the sharper knees at lower pressures in both Ln-PB isotherms indicate the predominance of narrower pores with more similar widths upon doping. Tb-PB has a narrower pore size distribution (PSD) than Eu-PB as evidenced by the sharp knee of its type I(a) isotherm in comparison to the flat knee of the type I(b) isotherm of the latter. The PSD of the xerogels (Fig. 3), calculated through the density functional theory methods, confirms that Eu-PB has a wider distribution of micropore sizes than Tb-PB and a lower volume of micropores with $\phi < 1$ nm because part of its porosity originates from narrow mesopores. Its maximum pore volume is centred at pore width values higher than those of Tb-PB or even TEOS-4.5 (Table S1). For Ln-CA materials, the decrease of surface areas and pore volumes upon doping is as substantial as to lead to xerogels that barely adsorb N_2, hence PSD analyses do not provide any reliable information.

To explore the ultramicroporosity ($\phi \leq 0.7$ nm) of Ln-AL, CO_2 isotherms (273 K) [27] and PSD values were also obtained, revealing opposite trends depending on the ligand (Fig. 4, semilogarithmic scale depiction in Fig. S4). Both Ln-PB materials adsorb slightly fewer amounts of CO_2 than TEOS-4.5, which originates from subtle reductions of the ultramicroporous volume upon doping, Tb enhancing this effect over Eu as observed for the N_2 isotherms. In contrast, the adsorption of CO_2 in Ln-CA xerogels is slightly higher than that of TEOS-2.7. This implies that Ln-CA are purely ultramicroporous rather than non-porous materials and that the lack of N_2 adsorption is caused by kinetic restraints to diffuse through the pores. PSD analyses show that the Ln-AL microporosity is mainly due to ultramicropores and micropores with 0.7 nm $< \phi \leq 1$ nm, although Ln-PB have a small contribution of wider pores ($\phi > 1$ nm). For Ln-CA materials, the ultramicroporous texture remains mostly unaffected upon doping, as revealed by the fact that the PSD curves are nearly identical to that of TEOS-2.7.

Overall, the adsorption data obtained with both probe molecules indicate that doping the XG matrix with Ln and AL noticeably affects the porous texture by reducing the pore volumes and specific surface areas and narrowing the pore diameters. For Ln-PB, it is worth noting that the Eu-containing xerogel adsorbs more N_2 and CO_2 than the Tb-analogue; Eu^{III} is larger than Tb^{III} due to the lanthanide contraction effect, thereby being more prone to form complexes with higher coordination number that would require larger pores to accommodate within the matrix.

3.2. Selection of OFS coating

After characterising the Ln-AL materials, the most-suited ligand for preparing a humidity sensor was selected among PB and CA based on both the luminescent and textural properties. Regarding luminescence, all materials exhibited optimal emission for both Ln ions. No free ligand emission was observed in any case, as observed for hydroxypicolinates. Concerning the porous texture, well-defined pore width values and narrow pore size distributions indicate that water molecules with an average size of 0.28 nm could freely enter the pores [28]. However, the purely ultramicroporous nature of Ln-CA xerogels and their lower adsorption capacity could cause kinetic drawbacks during the adsorption-desorption processes. Therefore, PB was found to be the best-suited AL for our purpose based on: i) PB is a tridentate ligand that effectively sensitises the Ln-luminescence and can saturate the coordination sphere to a degree in which molecular oscillators do not fully quench the emission through non-radiative decay; ii) the luminescent emission displays sharp peaks of enough intensity to be monitored; and iii) Ln-PB xerogels present the highest specific surface areas and the widest micropores among our homogeneous materials, while maintaining well-defined PSD, which could lead to a wider dynamic range of the sensor due to a higher adsorption capacity.

Once selected, the morphology of Ln-PB materials was studied by field-emission SEM (Fig. S5), finding smooth layered surfaces consistent

with their microporous nature, in contrast to the rougher surface of the micro-mesoporous TEOS-4.5. EDX spectroscopy was used to inspect the Ln distribution on XG surfaces, which led us to prepare Ln-PB xerogels with higher Ln concentration (3 wt%) due to the detection limit of the equipment. The lanthanide mapping (Fig. S6) confirms the homogeneous dopant distribution, which should remain also homogenous for a lower Ln quantity, such as that in Ln-PB xerogels. This assumption is supported by the powder XRD patterns (Fig. S7), which are dominated by a very broad signal centred at $2\theta = 22$–24° characteristic of amorphous silica. The absence of other sharp diffraction maxima indicates that the dopants must be well-dispersed within the XG matrix without forming crystalline aggregates or inducing any local order. The infrared spectra (Fig. S8, Table S2) show, besides the characteristic bands of XG matrices and siloxane assemblies within, additional signals confirming that the TEOS ethoxy groups are not fully hydrolysed (low-intensity C-H stretching peaks in the 2980–2850 cm^{-1} range) and that Ln-PB xerogels are hydrophilic according to the peaks at ca. 1650 (deformation of physisorbed water) and 3465 cm^{-1} (stretching of water molecules hydrogen-bonded to silanol groups). No signals from free ligands or Ln complexes are detected, other than a narrow peak at 1385 cm^{-1} assigned to nitrate anions from Ln precursors.

Three OFS were prepared: the reference sensor (OFSTEOS-4.5) using TEOS-4.5 and the working sensors (OFSEu-PB and OFSTb-PB) using Ln-PB coatings. The sensors were excited with a 280 nm LED to take advantage of the Stokes Shift and to prevent any overlap between the luminescent signals and the emission spectra in Fig. 5 were obtained (experimental set-up in Fig S1).

As expected, the reference OFSTEOS-4.5 does not show any luminescence in the studied range, consistent with the absence of any luminescent doping agents. The spectra of both OFSLn-PB show all the characteristic emission signals of each Ln ion, where the most intense bands were 546 nm and 617 nm for OFSTb-PB and OFSEu-PB, respectively. This observation is consistent with the PL spectra of Ln-PB monoliths discussed above. Nevertheless, the OFSTb-PB band at 546 nm is significantly more intense than that of OFSEu-PB at 617 nm, which shows also substantial overlapping with a signal at 627 nm. Thus, OFSTb-PB was selected for exploring its performance towards humidity variations, bearing in mind that the narrower, more intense, and better defined the emission band is, the better signal-noise ratio should be expected for the signal transduction.

3.3. Time-response curves for humidity

The OFSTb-PB response (deposited XG film thickness of 136
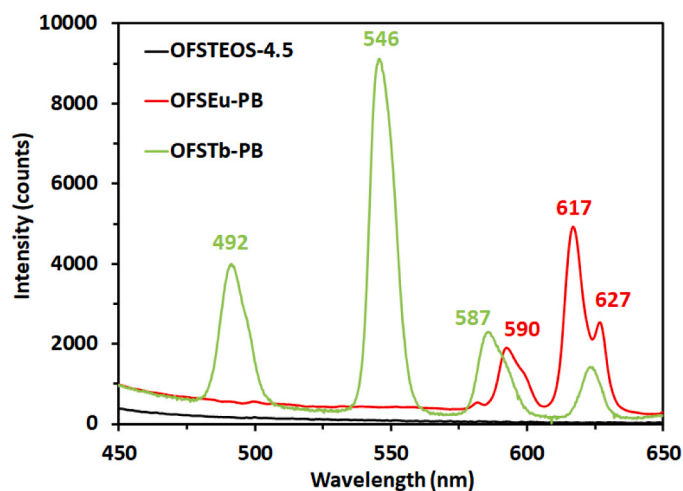

Fig. 5. Luminescence spectra ($\lambda_{exc} = 280$ nm) of OFSTEOS-4.5, OFSEu-PB and OFSTb-PB.

± 12 nm) versus relative humidity (RH) at different temperatures was studied using the configuration in Fig. S1. The sensor was exposed to 10 increasing/decreasing cycles of 20–90% RH (0.20–1.00 mM at 298 K, 0.28–1.40 mM at 303 K and 0.38–1.80 mM at 308 K) during 1 h per cycle to ensure time-stability. Fig. 6 displays the time-response curves at different water-vapour molar concentrations (C_{H_2O}) using the two most accurate RH cycles at each temperature. The interrogation of the sensor was carried out by tracking changes in the intensity of the emission peak centred at 546 nm, the value of which was obtained every minute from the emission spectrum. The intensity variation ($\Delta I = I - I_{ref}$) was estimated by subtracting the intensity measured at the lowest RH level (20%, I_{ref}) from the sampled values (I), normalising this variation by I_{ref} (see Eq. S1, section S1.3). Two hours were left between experiments at different temperatures to ensure the reference stability.

According to the response curves (Fig. 6), the sensor follows the C_{H_2O} setpoint (see Eq. S2 and S3, section S1.3) in all cycles. The variation in the OFSTb-PB response increases with C_{H_2O} due to the quenching of luminescence by water molecules [29]. Moreover, the dynamic intensity range of the sensor is also broadened when the temperature increases (from 0.129 at 298 K to 0.196 and 0.263 at 203 and 308 K, respectively). This behaviour can be explained by the higher vibration of the electrons

when the emission decreases, which in turn, favours alternative non-radiative deactivation pathways [30].

Table 1
Linear fitting parameters of OFSTb-PB calibration curves ($y = A + Bx$).

T^{a}	Linear intervals[b]	A	B	R^2	LoD[c]
K	mM	r.u.	mM^{-1}		mM
298[ads]	0.282–0.906	−0.025 ± 0.001	0.121 ± 0.002	0.993	0.022
298[des]	0.863–0.226	−0.040 ± 0.001	0.164 ± 0.002	0.995	0.018
303[ads]	0.292–0.957	−0.020 ± 0.000	0.070 ± 0.001	0.995	0.022
303[des]	0.839–0.300	−0.037 ± 0.001	0.117 ± 0.002	0.995	0.023
308[ads]	0.413–1.143	−0.022 ± 0.001	0.056 ± 0.001	0.988	0.048
308[des]	0.999–0.399	−0.047 ± 0.002	0.118 ± 0.002	0.992	0.038

[a] ads: adsorption, des: desorption.
[b] Linear water-vapour molar concentration ranges for the calibration curves.
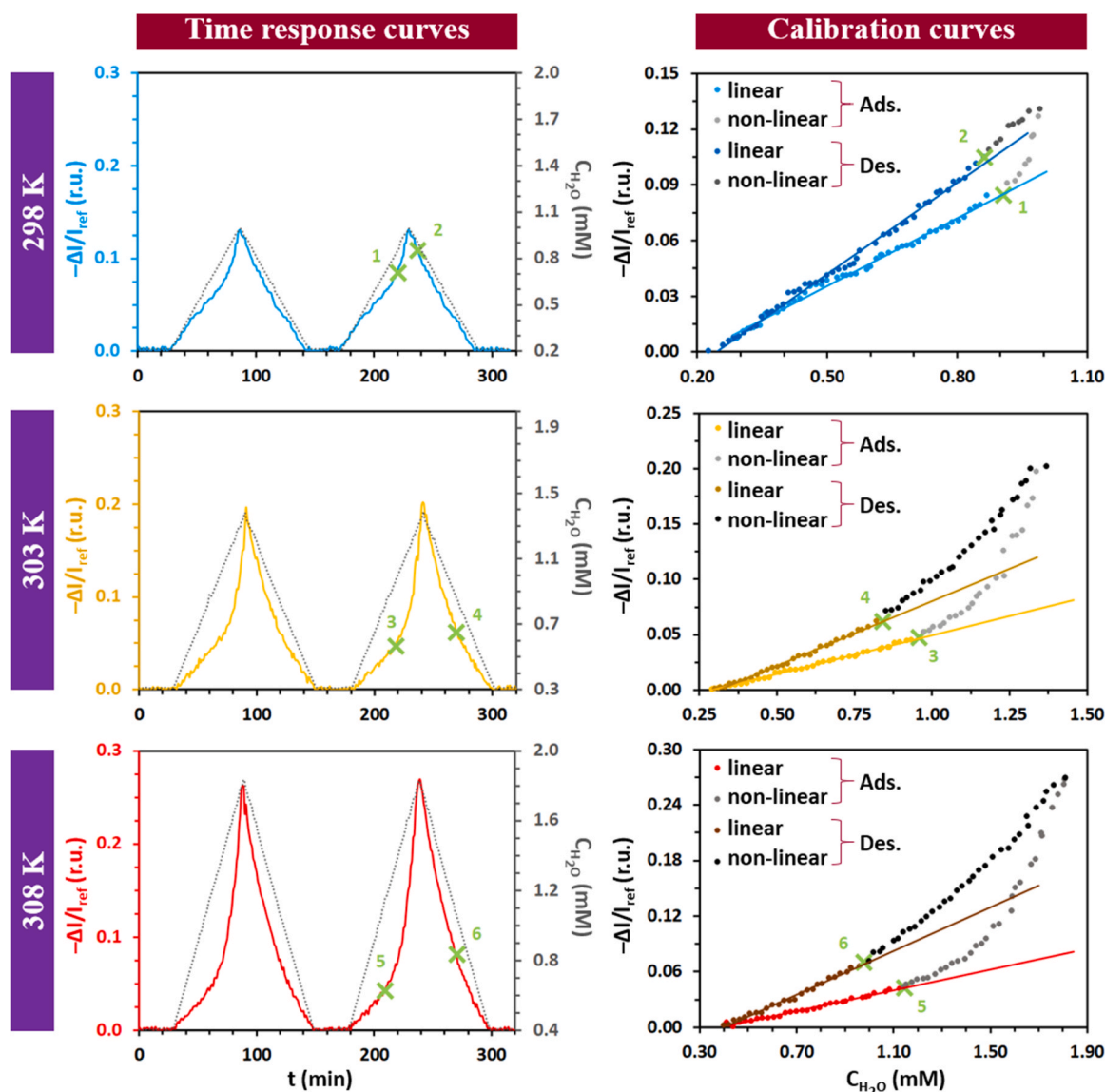[c] Limits of Detection (Eq. S4).

Fig. 6. Time-response curves for humidity and linear fitting of the OFSTb-PB calibration curves at different temperatures.

To study the linearity of the OFSTb-PB response with C_{H_2O}, the calibration curves in Fig. 6 were registered at the three working temperatures and their linear intervals analysed by calculating the inflection points 1–6 from the tangent of the curves where the latter started deviating from linearity (based on R^2). Table 1 compiles the linear fitting parameters and detection limits for each temperature, which are determined from the sensor sensitivity (fitting parameter B, see Eq. S4 in section S1.3). The dynamic behaviour displayed in Fig. 6 confirms that the sensor kinetics are able to follow relative humidity change rates of (at least) $\pm$ 0.02% per second, which expressed in water vapour molar concentration is equal to $\pm$ 13, $\pm$ 14 and $\pm$ 21 μM s^{-1} for 298, 303 and 308 K, respectively.

On the one hand, the OFSTb-PB response for the adsorption branches follows a linear trend at all temperatures up to C_{H_2O} values in the range from 0.91 mM at 298 K to 0.96 mM at 303 K and 1.14 mM at 308 K (RH = 81.7%, 64.3% and 57.6%, respectively). Beyond these values (points 1, 3 and 5 in Fig. 6), the response deviates abruptly from linearity to a third-grade polynomial (third-grade polynomial fittings compiled in Fig. S9 and Table S3). On the other hand, while desorption at 298 K is linear for almost the whole C_{H_2O} range, those at 303 and 308 K deviate from linearity at inflection points 4 and 6, as happened for adsorption. It is worth noting that temperature directly affects the linearity of the sensor response, with the inflection points appearing at higher C_{H_2O} as the temperature increases for the adsorption branches. The influence of the temperature on the sensor response can be mathematically modelled based on well-established analytical techniques [31], and we plan to apply such methods in the study of sensors with optimised XG coatings in terms of porous texture and surface chemistry. These improved sensors are currently in progress and will be reported in the near future. The performance of the present sensor is compared in Table 2 to those of several other humidity optical fibre probes that have been reported in the past few years. In this context, it is worth noting the lack of literature examples of humidity probes based on luminescence as the transduction method, such as our OFSTb-PB sensor.

The differences between the adsorption and desorption branches give rise to significant hysteresis loops, which widen as the temperature increases and relate to the retention of water molecules within the coating. To shed light on the adsorption-desorption mechanism of this film and to get information about the interaction of water molecules within the material pores, variable-temperature water-vapour isotherms

Fig. 7. Water-vapour isotherms of the Tb-PB monolith at different temperatures.

were registered for the Tb-PB monolith.

3.4. Water-vapour isotherms of Tb-PB

Fig. 7 and S10 depict the water-vapour isotherms recorded for the Tb-PB monolith at the three working temperatures to establish a correlation between the sensor response and the textural properties of its coating. The isotherms display a wide knee and a positive slope without *plateau*, the B point being noticeable. Therefore, they could be classified as type II, with a hysteresis loop H5. Tb-PB was found to be mainly microporous using the standard adsorbate N_2, but water molecules are smaller, more polar, and have higher kinetic energy in the adsorption process, hence lower values of partial pressures are required to fill the pores. Thus, the wide micropores for N_2 become mesopores for H_2O. The isotherms show that water molecules are indeed adsorbed following a linear trend at low partial pressures, but also that this behaviour changes when certain p/p_0 values are reached: 0.09 (298 K), 0.17 (303 K), and 0.27 (308 K). The hysteresis closure relates to a change in the adsorption mechanism from micropore filling to capillary condensation in the mesopores. The higher the temperature is, the higher the p/p_0 values needed for the hysteresis loop to close, a fact that agrees with the exothermic nature of the adsorption process [23], as well as with the Tb-PB hydrophilicity due to the interaction between adsorbed water molecules and silanol groups (Fig. S8).

Table 3 displays the thermal effect on several textural parameters

Table 2
Room-temperature performances of literature-reported optical fibre humidity probes compared to that of OFSTb-PB.

Material	Transduction	Range (%RH)	Sensitivity	Response Time	Ref.
None	WG Modes	30 - 70	0.23 dB / %RH	240 ms	[32]
PDMS[a]	Fabry Perot	30 - 80	11.39 nm / % RH	125 s	[33]
GO[b]	LPG	20 - 80	0.18 dB / %RH	n/a	[34]
ITO[c]	LMR	30 - 90	116 pm / %RH	n/a	[35]
Agarose	Fabry Perot	50 - 90	0.673 nm / % RH	60 ms	[36]
FIR-53[d]	Fabry Perot	10 - 90	315 pm / %RH	323 s	[37]
GO[b]	Frequency	30 - 98	34.7 KHz / % RH	64.2 ms	[38]
GO[b]	Sagnac	36 - 78	340 pm / %RH	n/a	[39]
GO[b]	LMR	20 - 90	1.324 nm / % RH	160 ms	[40]
Tb-PB	Luminescence	20 - 90	1.71×10^{-3} r.u / %RH[e]	n/a	This work

[a] PDMS: polydimethylsiloxane.
[b] GO: graphene oxide.
[c] ITO: indium tin oxide.
[d] FIR-53: [Zn_2(tipa)$_2$OH](NO$_3$)$_3$·12H$_2$O MOF, where tipa = tris(4-(1H-imidazol-1-yl)phenyl)amine).
[e] Calculated from the adsorption branch sensitivity datum at 298 K (Table 3) using 0.0141 mM / %RH as the conversion factor.
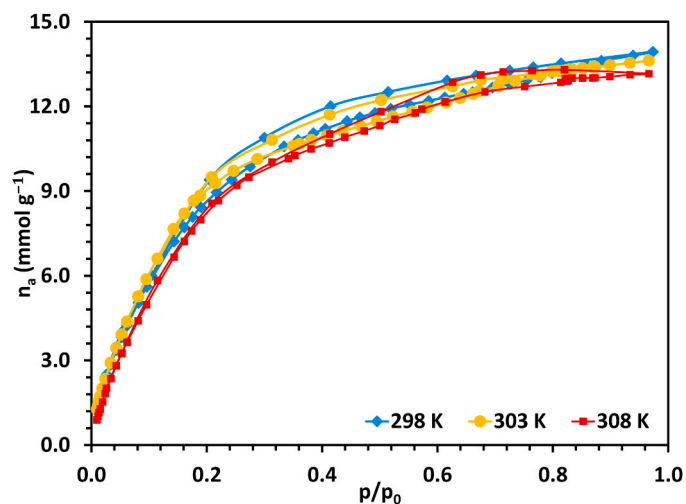
Table 3
Textural parameters determined from the Tb-PB water-vapour adsorption isotherms.

T	a_{BET}[a,b]	V_{micro}	V_{meso}[a,ca,d]	V_{total}	q_m[f]	E_c[a,ea,g]
K	m^2·g^{-1}	cm^3·g^{-1}			mmol·g^{-1}	kJ·mol^{-1}
298	694	0.15	0.09	0.24	8.9	8.3
303	669	0.15	0.08	0.24	8.9	8.0
308	659	0.13	0.10	0.24	8.8	7.6

[a] Using the H$_2$O isotherms.
[b] Specific surface area from the Brunauer–Emmett–Teller (BET) model (section S1.2).
[c] Micropore volume from the Dubinin-Raduskevich (DR) method (section S1.2).
[d] $V_{meso} = V_{total} - V_{macro} - V_{micro}$ (negligible macroporosity observed in the 0.8 < p/p_0 < 0.95 range).
[e] Total pore volume at p/p_0 = 0.95.
[f] Monolayer capacity from BET.
[g] Characteristic energy from DR.

determined from the water-vapour adsorption isotherms. These data confirm the presence of a significant mesoporous volume and show that the adsorption monolayer capacity (q_m) increases with temperature. This fact is consistent with the decrease in the characteristic adsorption energy (E_c) because the attraction forces between adsorption sites and water molecules become weaker as the temperature increases [41], thereby needing higher C_{H_2O} to reach the monolayer capacity. This phenomenon can explain both the filling of mesopores at higher p/p_0 values with increasing temperature, as well as the non-linear nature of the calibration curves beyond inflection points 1, 3, and 5 (Fig. 6). All these observations suggest that capillary condensation is a plausible mechanism in the pore filling. To confirm this hypothesis by comparing the strength of water physisorption in both systems, determining the isosteric enthalpies of adsorption (ΔH_{ads}) for both the Tb-PB monolith and the OFSTb-PB sensor became essential.

3.5. Isosteric enthalpies of adsorption

ΔH_{ads} is the differential change in energy when a tiny number of molecules are transferred at constant pressure, temperature, and specific surface area of the adsorbent from the bulk gas phase to the adsorbed phase [42]. It is a crucial parameter in adsorption processes and is further used to gain deeper insights into the adsorbate-adsorbent interactions, which are classified as physisorption (weak interactions) and chemisorption (strong interactions) [43]. Therefore, the sensor response towards humidity could be explained in terms of analyte-adsorbent interactions by a mere comparison between ΔH_{ads} of the XG monolith and that of the XG coating. The Clausius-Clapeyron equation (Eq. 1) was used to determine the sensor ΔH_{ads} (kJ·mol^{-1}) upon assuming that

adsorption is an exothermic process [23]. This equation specifies the temperature dependence of the vapour pressure in phase transitions like capillary condensation (gas-liquid):

$$\ln P = \frac{\Delta H_{ads}}{R} \times \frac{1}{T} + K \qquad (1)$$

where P = pressure (kPa), R = ideal gas constant (kJ·mol^{-1}·K^{-1}), T = temperature (K), and K = constant (y-intercept). To obtain the P_{H_2O} values assuming ideal gas conditions, a least-squared adjustment was performed for the data from both the time-response curves of the sensor OFSTb-PB (Table S3) and the water-vapour adsorption isotherms of the monolith Tb-PB (Table S4 and Fig. S11). Thereafter, $\ln P_{H_2O}$ was plotted against $1/T$, thus obtaining isosteres in the ranges $-\Delta I/I_{ref}$ = 0.03–0.18 range for OFSTb-PB and n_a = 1.5–10.0 (n_a: mmols of water adsorbed per gram of material) for Tb-PB. The isostere slopes allowed the determination of the corresponding ΔH_{ads} values, which were represented as a function of $-\Delta I/I_{ref}$ and n_a to study the strength of the adsorbate-adsorbent binding energy as C_{H_2O} increases.

Fig. 8 shows that ΔH_{ads} becomes less negative with increasing $-\Delta I/I_{ref}$ until reaching a *plateau* at -34.5 kJ·mol^{-1}. This fact is consistent with a less exothermic process as more water molecules are adsorbed. Values higher than the theoretical one corresponding to water condensation ($\Delta H_{cond} = -40.7$ kJ·mol^{-1}, [44]) agree with the predominance of condensation (adsorbate-adsorbate interactions) over adsorption (adsorbate-adsorbent interactions). Below $-\Delta I/I_{ref}$ = 0.07, the ΔH_{ads} magnitude remains above the energetic threshold given by ΔH_{cond}, which indicates a mechanism of physisorption in the micropores ruling the linear range of the OFSTb-PB response in the calibration curves (Fig. 6). Conversely, ΔH_{ads} is observed to be less negative than ΔH_{cond}
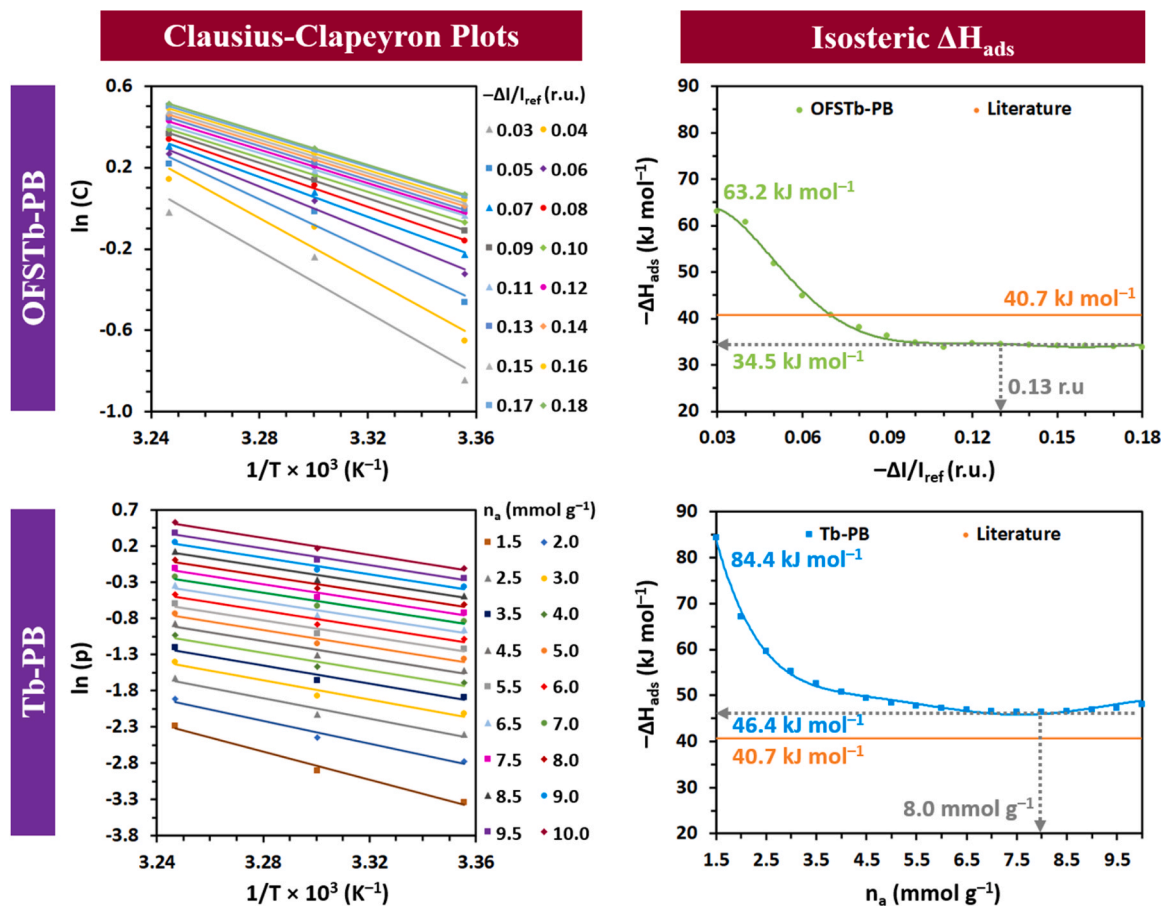

Fig. 8. Left: Clausius-Clapeyron plots for the OFSTb-PB response towards humidity changes ($-\Delta I/I_{ref}$ = 0.03–0.18) and for the Tb-PB water-vapour adsorption isotherms (n_a = 1.5–10.0 mmol·g^{-1}). Right: Isosteric enthalpies of adsorption calculated for the sensor and the monolith.

when $-\Delta I/I_{ref}$ is above 0.07, and this fact suggests that the inflection points leading to non-linear trends in the sensor calibration curves match with the beginning of capillary condensation in the mesopores.

Fig. 8 also depicts the correlation between ΔH_{ads} calculated for Tb-PB and the amount of adsorbed water (n_a). In close analogy to what has been commented above, ΔH_{ads} gradually increases with n_a to reach a *plateau* at n_a 7.5–8.0 mmol·g^{-1}. This value is similar to those calculated for the monolayer capacities (q_m) from the water adsorption isotherms (Table 3) and correlates in the graph with $\Delta H_{ads} = -46.4$ kJ·mol^{-1}. Although ΔH_{ads} in the *plateau* does not surpass ΔH_{cond}, this phenomenon can be expected when considering the morphological difference between the sensor coating (a thin film of the material) and a monolith (the bulk material), as the total volume of pores is higher in the latter. The key parameter to consider is the ΔH_{ads} increment until reaching the *plateau*, which is comparable in both cases (28.7 kJ·mol^{-1} for the coating vs. 38.0 kJ·mol^{-1} for the monolith). The information extracted from comparing both isosteric enthalpies of adsorption reinforces the hypothesis that the loss of linearity in the OFSTb-PB response originates from the beginning of capillary water condensation in the mesopores.

4. Conclusions

Two series of Eu^{III}- or Tb^{III}-doped silica xerogels were prepared by the sol-gel method and their luminescence was sensitised using eight pyridine-based antenna ligands. Out of a catalogue of 16 resulting materials, the xerogel Tb-PB (sensitised with the 2,2′-(4-(2-Ethoxyethoxy) pyridine-2,6-diyl)bis(4,5-dihydrooxazole) ligand) showed the most-suited luminescence and textural properties for a coating in a humidity optical fibre sensor.

The sensor response showed linearity until certain values of water-vapour molar concentration (C_{H_2O}), beyond which shifted to polynomial. Comparing the sensor calibration curves with the water-vapour adsorption isotherms of the bulk material recorded at three working temperatures and calculating their isosteric enthalpies of adsorption (ΔH_{ads}), the linear-to-polynomial shift was found to originate from capillary condensation of water molecules in the mesopores. When the membrane is exposed to low C_{H_2O}, the molecules first interact with the hydrophilic silanol groups on the micropore surface and quench the luminescence linearly while ΔH_{ads} increases, making the adsorption process less exothermic. Once C_{H_2O} is high enough to complete the monolayer, water molecules are physisorbed forming multilayers in the mesopores due to their larger size compared to micropores. When $\Delta H_{ads} \geq \Delta H_{cond}$, water molecules condense, which critically eases their contact with the luminophores, causing an abrupt decay in the luminescence that breaks the linearity of the sensor response.

This work has established a correlation between the response of a luminescent probe and its textural and proposes a plausible adsorption mechanism to explain the non-linear response of the sensor based on capillary condensation within mesopores. The knowledge acquired from this investigation is of paramount importance for improving, based on the porous texture, the design of materials that will be used as coatings where the analyte interacts with the sensor.

CRediT authorship contribution statement

Cruz-Quesada Guillermo: Investigation, Writing – original draft. **Rosales-Reina Beatriz:** Investigation, Writing – original draft. **López-Torres Diego:** Investigation, Writing – original draft. **Reinoso Santiago:** Funding acquisition, Writing – review & editing. **López-Ramón María Victoria:** Writing – review & editing. **Elosua César:** Data curation, Investigation, Methodology, Writing – review & editing. **Espinal-Viguri Maialen:** Investigation, Methodology, Resources, Writing – review & editing. **Garrido Julián J.:** Conceptualization, Funding acquisition, Project administration, Supervision, Writing – review & editing. **Arzamendi Gurutze:** Data curation, Formal analysis.

Declaration of Competing Interest

The authors declare that they have no known competing financial interests or personal relationships that could have appeared to influence the work reported in this paper.

Data availability

The data presented in this study are available on request from the corresponding author.

Appendix A. Supporting information

Full experimental section; photographs under UV light, FT-IR spectra, PXRD patterns, details of N_2, CO_2 and H_2O isotherms, SEM micrographs and EDX mappings of Ln-AL materials; fittings of OFSTb-PB calibration curves; details and fittings of Tb-PB water-vapour adsorption isotherms.

Appendix B. Supporting information

Supplementary data associated with this article can be found in the online version at doi:10.1016/j.snb.2024.135369.

References

[1] A. de Bettencourt-Dias, P.S. Barber, S. Bauer, A water-soluble Pybox derivative and its highly luminescent lanthanide ion complexes, J. Am. Chem. Soc. 134 (2012) 6987–6994, https://doi.org/10.1021/ja209572m.

[2] J.R. Lakowicz. Principles of Fluorescence Spectroscopy, third ed., Springer, New York, 2006 https://doi.org/10.1007/978-0-387-46312-4.

[3] N. de Acha, C. Elosua, I. Matias, F.J. Arregui, Luminescence-based optical sensors fabricated by means of the layer-by-layer nano-assembly technique, Sensors 17 (2017) 2826, https://doi.org/10.3390/s17122826.

[4] H.-S. Lv, S.-Y. Huang, B.-X. Zhao, J.-Y. Miao, A new rhodamine B-based lysosomal pH fluorescent indicator, Anal. Chim. Acta 788 (2013) 177–182, https://doi.org/10.1016/j.aca.2013.06.038.

[5] Y. Li, Temperature and humidity sensors based on luminescent metal-organic frameworks, Polyhedron 179 (2020) 114413, https://doi.org/10.1016/j.poly.2020.114413.

[6] X. Pang, T. Yu, F. Shen, X. Yu, Y. Li, Fluorescence sensing of fluoride ions and N,N-dimethylformamide by novel luminescent lanthanide(III) xerogels, J. Lumin. 204 (2018) 169–175, https://doi.org/10.1016/j.jlumin.2018.08.004.

[7] D. Ross, M. Gaitan, L.E. Locascio, Temperature measurement in microfluidic systems using a temperature-dependent fluorescent dye, Anal. Chem. 73 (2001) 4117–4123, https://doi.org/10.1021/ac010370l.

[8] J. Yan, H. Wang, Y. Zheng, X. Huang, H. Meng, C. Tan, A novel dew point measurement system based on the thermal effect of humidity sensitive thin film, Measurement 187 (2022) 110248, https://doi.org/10.1016/j.measurement.2021.110248.

[9] D.S. Ballantine, H. Wohltjen, Optical waveguide humidity detector, Anal. Chem. 58 (1986) 2883–2885, https://doi.org/10.1021/ac00126a068.

[10] D. Bridgeman, J. Corral, A. Quach, X. Xian, E. Forzani, Colorimetric humidity sensor based on liquid composite materials for the monitoring of food and pharmaceuticals, Langmuir 30 (2014) 10785–10791, https://doi.org/10.1021/la502593g.

[11] M.M.F. Choi, O.L. Tse, Humidity-sensitive optode membrane based on fluorescent dye immobilized in gelatin film, Anal. Chim. Acta 378 (1999) 127–134, https://doi.org/10.1016/S0003-2670(98)00614-X.

[12] M. Soltani Firouz, K. Mohi-Alden, M. Omid, A critical review on intelligent and active packaging in the food industry: research and development, Food Res. Int. 141 (2021) 110113, https://doi.org/10.1016/j.foodres.2021.110113.

[13] L. Fang, G. Clausen, P.O. Fanger, Impact of temperature and humidity on chemical and sensory emissions from building materials, Indoor Air 9 (1999) 193–201, https://doi.org/10.1111/j.1600-0668.1999.t01-1-00006.x.

[14] A. Sathish, B.R. Smith, R.C. Sims, Effect of moisture on in situ transesterification of microalgae for biodiesel production, J. Chem. Technol. Biotechnol. 89 (2014) 137–142, https://doi.org/10.1002/jctb.4125.

[15] J. Estella, P. de Vicente, J.C. Echeverría, J.J. Garrido, A fibre-optic humidity sensor based on a porous silica xerogel film as the sensing element, Sens. Actuators B Chem. 149 (2010) 122–128, https://doi.org/10.1016/j.snb.2010.06.012.

[16] C. Zhao, D. Liu, G. Xu, J. Zhou, X. Zhang, C. Liao, Y. Wang, Recent advances in fiber optic sensors for respiratory monitoring, Opt. Fiber Technol. 72 (2022) 103000, https://doi.org/10.1016/j.yofte.2022.103000.

[17] F. Lu, R. Wright, P. Lu, P.C. Cvetic, P.R. Ohodnicki, Distributed fiber optic pH sensors using sol-gel silica based sensitive materials, Sens. Actuators B Chem. 340 (2021) 129853, https://doi.org/10.1016/j.snb.2021.129853.

[18] L. Sun, Y. Semenova, Q. Wu, D. Liu, J. Yuan, X. Sang, B. Yan, K. Wang, C. Yu, G. Farrell, Investigation of humidity and temperature response of a silica gel coated microfiber coupler, IEEE Photonics J. 8 (2016) 6805410, https://doi.org/10.1109/JPHOT.2016.2619479.

[19] J. Estella, J.C. Echeverría, M. Laguna, J.J. Garrido, Silica xerogels of tailored porosity as support matrix for optical chemical sensors. Simultaneous effect of pH, ethanol:TEOS and water:TEOS molar ratios, and synthesis temperature on gelation time, and textural and structural properties, J. Non Cryst. Solids 353 (2007) 286–294, https://doi.org/10.1016/j.jnoncrysol.2006.12.006.

[20] C. Elosua, F.J. Arregui, I. del Villar, C. Ruiz-Zamarreño, J.M. Corres, C. Bariain, J. Goicoechea, M. Hernaez, P.J. Rivero, A.B. Socorro, A. Urrutia, P. Sanchez, P. Zubiate, D. Lopez-Torres, N. de Acha, J. Ascorbe, A. Ozcariz, I.R. Matias, Micro and nanostructured materials for the development of optical fibre sensors, Sensors 17 (2017) 2312, https://doi.org/10.3390/s17102312.

[21] N. De Acha, C. Elosúa, F.J. Arregui, Development of an aptamer based luminescent optical fiber sensor for the continuous monitoring of Hg^{2+} in aqueous media, Sensors 20 (2020) 2372, https://doi.org/10.3390/s20082372.

[22] J.C. Echeverría, M. Faustini, J.J. Garrido, Effects of the porous texture and surface chemistry of silica xerogels on the sensitivity of fiber-optic sensors toward VOCs, Sens. Actuators B Chem. 222 (2016) 1166–1174, https://doi.org/10.1016/j.snb.2015.08.010.

[23] J.C. Echeverría, I. Calleja, P. Moriones, J.J. Garrido, Fiber optic sensors based on hybrid phenyl-silica xerogel films to detect n-hexane: determination of the isosteric enthalpy of adsorption, Beilstein J. Nanotechnol. 8 (2017) 475–484, https://doi.org/10.3762/BJNANO.8.51.

[24] P.C.R. Soares-Santos, H.I.S. Nogueira, V. Félix, M.G.B. Drew, R.A. Sá Ferreira, L. D. Carlos, T. Trindade, Novel lanthanide luminescent materials based on complexes of 3-hydroxypicolinic acid and silica nanoparticles, Chem. Mater. 15 (2003) 100–108, https://doi.org/10.1021/cm021188j.

[25] J.-C.G. Bünzli, S.V. Eliseeva, Basics of lanthanide photophysics, in: P. Hänninen, H. Härmä (Eds.), Lanthanide Luminescence: Photophysical, Analytical and Biological Aspects, Springer-Verlag, Berlin Heidelberg, 2010, pp. 1–45, https://doi.org/10.1007/4243_2010_3.

[26] M. Thommes, K. Kaneko, A.V. Neimark, J.P. Olivier, F. Rodriguez-Reinoso, J. Rouquerol, K.S.W. Sing, Physisorption of gases, with special reference to the evaluation of surface area and pore size distribution (IUPAC Technical Report), Pure Appl. Chem. 87 (2015) 1051–1069, https://doi.org/10.1515/pac-2014-1117.

[27] J. Garrido, A. Linares-Solano, J.M. Martin-Martinez, M. Molina-Sabio, F. Rodriguez-Reinoso, R. Torregrosa, Use of nitrogen vs. carbon dioxide in the characterization of activated carbons, Langmuir 3 (1987) 76–81, https://doi.org/10.1021/la00073a013.

[28] M.F. Chaplin, Structure and properties of water in its various states. in: Encyclopedia of Water: Science, Technology, and Society, John Wiley & Sons, 2019, pp. 1–19, https://doi.org/10.1002/9781119300762.wsts0002.

[29] G.E. Dobretsov, T.I. Syrejschikova, N.V. Smolina, On mechanisms of fluorescence quenching by water, Biophysics 59 (2014) 183–188, https://doi.org/10.1134/S0006350914020079.

[30] M. Hasegawa, H. Ohmagari, H. Tanaka, K. Machida, Luminescence of lanthanide complexes: from fundamental to prospective approaches related to water- and molecular-stimuli, J. Photochem. Photobiol. C 50 (2022) 100484, https://doi.org/10.1016/j.jphotochemrev.2022.100484.

[31] C. He, S. Korposh, R. Correia, L. Liu, B.R. Hayes-Gill, S.P. Morgan, Optical fibre sensor for simultaneous temperature and relative humidity measurement: towards absolute humidity evaluation, Sens. Actuators B Chem. 344 (2021) 130154, https://doi.org/10.1016/j.snb.2021.130154.

[32] J. Yan, D.N. Wang, Y. Ge, Y. Guo, B. Xu, A humidity sensor based on a whispering-gallery-mode resonator with an l-shaped open microcavity, J. Lightwave Technol. 40 (2022) 2651–2656, https://doi.org/10.1109/JLT.2021.3138737.

[33] H. Chen, C. Jiang, X. Zhu, X. Guo, H. Li, S. Sun, A parallel optical fiber Fabry–Perot interferometer for simultaneous measurement of relative humidity and

[34] Y.-T. Tsai, C.-W. Wu, L. Tsai, C.-C. Chiang, Application of graphene oxide-based, long-period fiber grating for sensing relative humidity, J. Lightwave Technol. 39 (2021) 4124–4130, https://doi.org/10.1109/JLT.2020.3006380.

[35] O. Fuentes, J.M. Corres, I.R. Matias, I.Del Villar, Generation of lossy mode resonances in planar waveguides toward development of humidity sensors, J. Lightwave Technol. 37 (2019) 2300–2306, https://doi.org/10.1109/JLT.2019.2902045.

[36] X. Ma, F. Zhao, B. Xu, C.L. Zhao, H. Chen, D.N. Wang, S. Jin, High-sensitivity and fast-response humidity sensor based on a simple fiber-tip interferometer with thin agarose gel coating, J. Lightwave Technol. 41 (2023) 6824–6830, https://doi.org/10.1109/JLT.2023.3289533.

[37] S. Liu, X. Zhang, Q. Wang, S. Chen, F. Wang, J. Wang, G. Wang, W. Yang, M. Huang, Integrated and robust Fabry–Perot humidity sensor based on metal–organic framework onto fiber-optic facet, IEEE Sens. J. 23 (2023) 12906–12914, https://doi.org/10.1109/JSEN.2023.3273905.

[38] K. Guo, J. He, H. Li, X. Xu, B. Du, S. Liu, Y. Chen, D. Ma, Y. Wang, G. Xu, Y. Wang, Polarimetric fiber laser for relative humidity sensing based on graphene oxide-coated D-shaped fiber and beat frequency demodulation, Opt. Express 30 (2022) 15998–16008, https://doi.org/10.1364/OE.457297.

[39] L. Li, Z. Wang, Q. Ma, M. Wang, Q. Wu, H. Chen, B. Peng, Sagnac ring humidity sensor with a melting cone based on graphene properties, IEEE Sens. J. 21 (2021) 16061–16065, https://doi.org/10.1109/JSEN.2021.3075443.

[40] M. Hernaez, B. Acevedo, A.G. Mayes, S. Melendi-Espina, High-performance optical fiber humidity sensor based on lossy mode resonance using a nanostructured polyethylenimine and graphene oxide coating, Sens. Actuators B Chem. 286 (2019) 408–414, https://doi.org/10.1016/j.snb.2019.01.145.

[41] G. Sang, S. Liu, D. Elsworth, Water vapor sorption properties of Illinois shales under dynamic water vapor conditions: experimentation and modeling, Water Resour. Res. 55 (2019) 7212–7228, https://doi.org/10.1029/2019WR024992.

[42] P.W. Atkins, Adsorption at surfaces, in: in: Physical Chemistry, third ed., W. H. Freeman and Company, New York, 1986, pp. 770–777.

[43] Z. Du, X. Nie, S. Deng, L. Zhao, S. Li, Y. Zhang, J. Zhao, Comparative analysis of calculation method of adsorption isosteric heat: case study of CO_2 capture using MOFs, Microporous Mesoporous Mater. 298 (2020) 110053, https://doi.org/10.1016/j.micromeso.2020.110053.

[44] E. Brini, C.J. Fennell, M. Fernandez-Serra, B. Hribar-Lee, M. Lukšič, K.A. Dill, How water's properties are encoded in its molecular structure and energies, Chem. Rev. 117 (2017) 12385–12414, https://doi.org/10.1021/acs.chemrev.7b00259.

Guillermo Cruz-Quesada received his B.Sc. and M.Sc. degrees in Chemistry from the University of Jaen (Spain, 2016 and 2017, respectively). He is currently a Ph.D. in the inorganic chemistry research group of the Science Department of the Public University of Navarre UPNA (Spain). His research interests include hybrid silica xerogels, xerogels doped with lanthanides, gas sensing, and the development of silica-based photocatalysts.

Beatriz Rosales-Reina received her B.Sc. degree in Chemical Engineering from the University of Granada (Spain, 2018) and a M.Sc. degree in Chemical Engineering from the University of Málaga (Spain, 2020). She is currently a Ph.D. student at the Public University of Navarra UPNA (Spain). Her research interests include optical fibre sensors and siliceous materials.

Diego López-Torres received his B.Sc. degree in Electrical and Electronic Engineering and a M.Sc degree in Communications from the Public University of Navarre (Spain, 2013 and 2014 respectively), and his Ph.D. degree in 2019. In 2013, he joined the Sensors group in the Department of Electrical, Electronic and Communications Engineering, becoming a Lecturer in this department in 2023. His research interests include chemical fibre optic sensors, photonic crystal fibres and nanostructured materials.

Santiago Reinoso received his M.Sc. degree in Materials Science (2002) and his Ph.D. degree in Inorganic Chemistry (2005) from the University of the Basque Country UPV/EHU (Spain). After postdoctoral stays at Constructor University (Germany) and the Institute for Molecular Science - University of Valencia (Spain), he joined the Public University of Navarre in 2017, where he now holds the position of Lecturer. His research interests focus on the design of smart materials based on the integration of molecular coordination species including polyoxometalates into functional solid supports.

María Victoria López-Ramón is a Full Professor of Inorganic Chemistry at the University of Jaén (Spain). She received her Ph.D. in Chemistry at the University of Granada (Spain) and obtained the Ph.D. Extraordinary Award in Chemistry. She has been a postdoctoral researcher at the University of Cambridge (UK) for two years. Her most highlighted inputs developed in her research lines are the synthesis and physicochemical characterisation of carbon-based adsorbents and photocatalysts from different raw materials, and the synthesis and characterisation of nanomaterials and their application as catalysts in advanced oxidation processes.

Gurutze Arzamendi is a Full Professor of Chemical Engineering at the Public University of Navarre (Spain). Her research work since 1988 has been carried out in various fields of Chemical Engineering such as chemical processes, especially those that lead to the production of renewable fuels and polymeric materials. She has recently expanded her research towards ceramic materials and their novel applications, is a co-author of more than 100 international scientific publications resulting in an h-index of 41.

César Elosúa received his M.Sc. and Ph.D. degrees in Telecommunication Engineering from the Public University of Navarre UPNA (Spain, 2004 and 2010 respectively), as well as another M.Sc degree in Biomedical Engineering in 2013. He has joined as short stay researcher groups from the University of Limerick, City University of London, University of Strasbourg and FORTH. Since 2022, he holds a permanent position as a Senior Lecturer at UPNA. His research interests include optical fibre sensors to detect biochemical magnitudes, sensor networks, nanomaterials, electronics and data processing.

Maialen Espinal-Viguri received her B.Sc. degree in Chemistry from the University of Zaragoza (Spain, 2009) and her M.Sc. and Ph.D. degrees from the University of Oviedo (Spain, 2015). After two postdoctoral stays at the University of Bath (UK) as a Research Associate and a Marie Curie Postdoctoral Fellow, she joined the Public University of Navarre UPNA (Spain, 2020). Since 2021 she is a Lecturer in Organic Chemistry, and her research interests focus on the design of organic and organometallic catalysts for asymmetric synthesis and the development of new hybrid silica materials for sensing and photocatalysis.

Julián J. Garrido received his B.Sc. in Chemistry from the University of Granada (Spain, 1977). He joined the Inorganic Chemistry Department at the University of Alicante (Spain), where he received his Ph.D. in Chemistry (1984). From 1984 until 1989, he was a member of the Engineering School at the University of Navarra (San Sebastián, Spain). In 1989, he joined the Department of Applied Chemistry at the Public University of Navarra (Spain), where he is currently a Full Professor of Inorganic Chemistry. His research interests include the synthesis and characterisation of porous silica materials and optical fibre sensors.